Available online at www.sciencedirect.com
ScienceDirect
Trans. Nonferrous Met. Soc. China 34(2024) 2943−2958

Transactions of
Nonferrous Metals
Society of China
www.tnmsc.cn

Improvement of ionic conductivity of solid polymer electrolyte based on Cu−Al bimetallic metal-organic framework fabricated through molecular grafting

Liu-bin SONG[1,2#], Tian-yuan LONG[1#], Min-zhi XIAO[1], Min LIU[3],
Ting-ting ZHAO[1,2], Yin-jie KUANG[1,2], Lin JIANG[1], Zhong-liang XIAO[1,2]

1. College of Chemistry and Chemical Engineering, Changsha University of Science and Technology, Changsha 410114, China;
2. Hunan Provincial Key Laboratory of Materials Protection for Electric Power and Transportation, Changsha University of Science and Technology, Changsha 410114, China;
3. College of New Energy, Ningbo University of Technology, Ningbo 315336, China

Received 4 March 2023; accepted 5 September 2023

Abstract: A composite solid electrolyte comprising a Cu−Al bimetallic metal-organic framework (CAB), lithium salt (LiTFSI) and polyethylene oxide (PEO) was fabricated through molecular grafting to enhance the ionic conductivity of the PEO-based electrolytes. Experimental and molecular dynamics simulation results indicated that the electrolyte with 10 wt.% CAB (PL-CAB-10%) exhibits high ionic conductivity (8.42×10^{-4} S/cm at 60 °C), high Li^+ transference number (0.46), wide electrochemical window (4.91 V), good thermal stability, and outstanding mechanical properties. Furthermore, PL-CAB-10% exhibits excellent cycle stability in both Li−Li symmetric battery and Li/PL-CAB-10%/$LiFePO_4$ asymmetric battery setups. These enhanced performances are primarily attributable to the introduction of the versatile CAB. The abundant metal sites in CAB can react with $TFSI^-$ and PEO through Lewis acid–base interactions, promoting LiTFSI dissociation and improving ionic conductivity. Additionally, regular pores in CAB provide uniformly distributed sites for cation plating during cycling.

Key words: polyethylene oxide; Cu−Al bimetallic metal-organic framework; solid lithium metal battery; molecular grafting; ionic conductivity

1 Introduction

Lithium-ion batteries (LIBs) are applied in various electronic products, electric vehicles, and large-scale energy storage systems owing to their lightweight characteristics and good cyclic stability [1−3]. However, conventional liquid LIBs employ highly volatile and flammable organic electrolytes, leading to inadequate stability, low ion selectivity and significant safety hazards [4−6]. Furthermore, the limited theoretical capacity of liquid LIBs fails to satisfy the high energy density requirements of advanced applications [7,8]. By contrast, solid-state batteries (SSBs) exhibit higher energy density and are safer and more suitable for high-energy storage devices [9−11]. However, the commercialization of SSBs is hindered by the low ionic conductivity of solid electrolytes (SEs), and unsatisfactory interfacial contact between the electrolyte and the electrode [12−14]. Thus, most studies on SSBs have primarily focused on

---

[#] Liu-bin SONG and Tian-yuan LONG contributed equally to this work

Corresponding author: Min LIU, E-mail: liumin@nbut.edu.cn;
Zhong-liang XIAO, E-mail: xiaozhongliang@163.com

DOI: 10.1016/S1003-6326(24)66587-8

improving the ionic conductivity of SEs and the electrolyte−electrode interface contact.

Solid-state polymer electrolytes (SPEs), particularly, polyethylene oxide (PEO), have attracted extensive attention owing to their high flexibility, high interfacial compatibility, and ease of preparation [15,16]. However, the inferior mechanical strength and low ionic conductivity of SPEs restrict their practical application [17−19]. Researchers have attempted to address these issues through approaches such as cross-linking [14], copolymerization [20,21], and filler incorporation [22−24]. Among various methods, adding fillers (TiO_2 [25], SiO_2 [26], Al_2O_3 [27], $Mg_2B_2O_5$ [28], $BaTiO_3$ [29], and $Gd_{0.1}Ce_{0.9}O_{1.95}$ [30]) to prepare composite SPEs results in the most substantial improvements in the mechanical strength and ionic conductivity of composite SPEs. Nonetheless, incorporating inorganic fillers may deteriorate the interfacial contact and stability of SPEs [31].

Being composed of metal ions and organic ligands, metal-organic frameworks (MOFs) are extensively used to modify SPEs owing to their rich porosity, large specific surface area, and inorganic–organic hybrid properties [32−34]. Compared with binary metal oxides, bimetallic MOFs offer several benefits for SPEs, which can be summarized as follows. Firstly, the metal content of bimetallic MOFs can be varied to accurately tune their physicochemical and electrochemical properties, including stability and conductivity [35,36]. Secondly, the controllable porous structures of bimetallic MOFs serve as ion sieves that preferentially facilitate cation transfer [37]. Thirdly, the large specific surface area of bimetallic MOFs promotes sufficient contact with other components [37,38]. Fourthly, the regular pores of bimetallic MOFs provide uniformly distributed metal sites, ensuring the uniformity of cation plating and the formation of stable interfacial layers during cycling, thus enhancing the cycle stability of SSBs [37,39]. Moreover, bimetallic MOFs with different active metal sites exhibit superior physicochemical properties and synergistic effects compared with their monometallic counterparts [40−42]. When selecting metal nodes for bimetallic MOFs, factors such as electronegativity, valency, Lewis acidity, and adsorption energy towards lithium salt anions must be considered [37]. For example, the high electronegativity of Cu^{2+} facilitates the formation of more covalent bonds with thermodynamic stability compared with other metals such as Mn^{2+}, Zn^{2+}, Cd^{2+}, and Pb^{2+} [43,44]. Because of its high valency and Lewis acidity, Al^{3+} effectively restricts the movement of lithium salt anions, thereby enhancing the dissociation of lithium bis(trifluoromethanesulphonyl) imide (LiTFSI) and improving the ionic conductivity of SPEs [45,46]. When appropriate metal nodes are selected, bimetallic MOFs with controllable structures and compositions can exhibit high stability, good conductivity, and exposed active sites [37]. At present most studies on bimetallic MOFs have been focused on their application in supercapacitors and electrocatalysis [47,48]; their applicability in SPEs has yet to be explored.

In the present study, molecular grafting was used to develop a novel and flexible PEO-based composite solid electrolyte film composed of Cu−Al bimetallic metal-organic framework (CAB) and LiTFSI to enhance the ionic conductivity and mechanical strength of SPEs. A series of composite solid electrolytes with varying amounts of CAB were prepared and characterized to investigate the effects of CAB content on the properties of SPEs. The influence mechanism of CAB in polymer electrolytes was analyzed through physicochemical characterization and molecular dynamics simulation (MDS). By using Cu−Al bimetallic MOF, this molecular grafting strategy offers an innovative approach for designing and developing high-performance SSBs.

2 Experimental

2.1 Synthesis of Cu−Al bimetallic MOFs materials

The Cu−Al bimetallic MOFs were synthesized through a hydrothermal method, as depicted in Fig. 1 and Fig. S1 in Supplementary Information. Firstly, 9 mmol of $Cu(NO_3)_2\cdot 3H_2O$ (AR, National Medicine) and 1.5 mmol of $Al(NO_3)_3\cdot 9H_2O$ (AR, National Medicine) were dissolved in ultrapure water and stirred magnetically until a homogeneous solution, referred to as Solution A, was obtained. Simultaneously, 6 mmol of homophthalic acid (H_3BTC, Macklin) and a small amount of cetyltrimethyl ammonium bromide (Macklin) were dissolved in anhydrous ethanol and stirred to form a transparent solution, referred to as Solution B. Subsequently, Solutions A and B were mixed and stirred for 30 min, then transferred to a Teflon-lined stainless-steel autoclave and heated at 120 °C for 24 h. The resulting precipitate was washed by centrifugation with ethanol and ultrapure water to obtain a light blue crystallite, which was then dried in a vacuum drying oven at 100 °C for 12 h. The dried blue crystallite was ground into a powder and activated in a vacuum drying oven at 150 °C to obtain Cu−Al bimetallic MOFs.

2.2 Preparation of composite solid electrolyte

As depicted in Fig. 2, the Cu−Al bimetallic MOFs, featuring abundant and highly Lewis acidic sites, reacted with the oxygen in PEO and $TFSI^-$ anions to form a composite solid electrolyte. Firstly, 0.4 g of LiTFSI (99.99%, Aladdin), 0.92 g of poly(propylene oxide) (PEO, relative molecular mass of 6×10^5, Macklin) and the desired amount of CAB were weighed and dissolved to 20 mL of anhydrous acetonitrile solution (AR, National Medicine). The mixture was stirred until complete dissolution. The resulting solution was poured into a container lined with a Teflon membrane and allowed to the rest 24 h to ensure that the acetonitrile solvent evaporated. Subsequently, it was transferred to a vacuum drying oven at 40 °C for 12 h to remove any residual solvent. The resulting solid electrolyte film was obtained and cut into small discs with a diameter of 19 mm for cell assembly. A control sample composed of the PEO polymer electrolyte without CAB was prepared. The composite electrolytes with mass fractions of CAB (0%, 1%, 5%, 10%, 15%) were denoted as PL, PL-CAB-1%, PL-CAB-5%, PL-CAB-10%, and PL-CAB-15%, respectively. All these processes were conducted in an Ar-filled glove box.

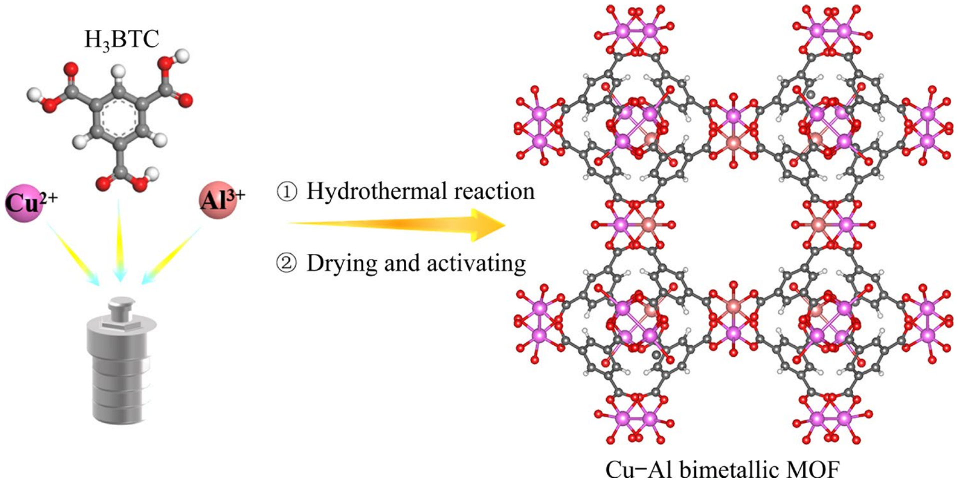

Fig. 1 Schematic diagram of fabrication of Cu−Al bimetallic MOF

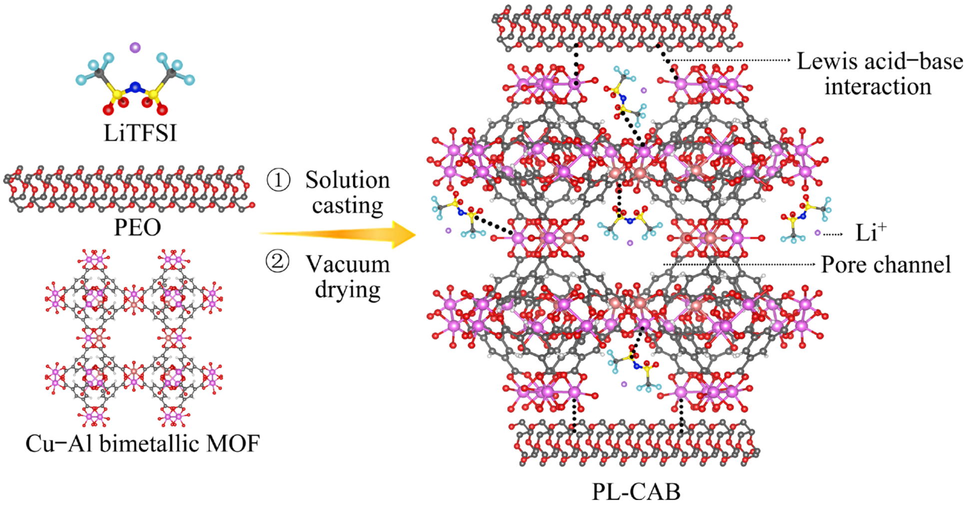

Fig. 2 Schematic diagram of synthesis of PL-CAB

3 Results and discussion

3.1 Physicochemical properties of Cu−Al bimetallic MOF

The crystal structures of the synthesized materials were examined using X-ray diffraction (XRD). As depicted in Fig. 3, the characteristic peaks of the synthesized materials resembled those of Cu-based MOF (HKUST-1) reported in previous studies [49,50], indicating the consistency in the crystal structure. Furthermore, no impurity peaks associated with Al compounds were observed in the spectra, suggesting the successful incorporation of the Al element into the crystal structure of HKUST-1 without disrupting the original arrangement of the crystal structure.

The microcosmic morphology of CAB was characterized using scanning electron microscopy (SEM), as illustrated in Fig. 4(a). The synthesized material exhibited a regular octahedral shape with a side length of approximately 40 μm. A closer inspection of the partially magnified SEM image (Fig. 4(b)) revealed that the octahedron was formed by self-assembled tiny primary particles, resulting in a porous structure. This porous structure enhanced the contact area with the polymer electrolyte, while the exposed metal active sites on the pore walls of CAB facilitated the binding of lithium salt anions in the pore channels. This binding promotes the transport of Li^+ along the interfacial channels formed between PEO and the CAB filler. Energy spectrum analysis revealed that Cu, Al, and O were uniformly distributed throughout the octahedral CAB rather than being aggregated at specific locations, confirming that the Cu−Al bimetallic MOF was successfully synthesized using the hydrothermal method.

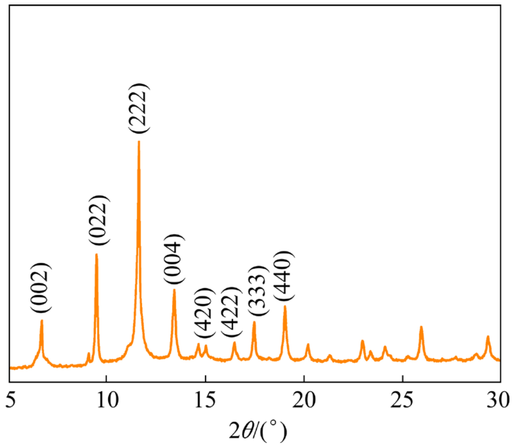

Fig. 3 XRD pattern of Cu−Al bimetallic MOF

3.2 Physicochemical properties of composite solid electrolytes

The incorporation of CAB can reduce the crystallized region of the PEO matrix and enhance Li^+ migration ability, as indicated by XRD and differential scanning calorimetry (DSC) results. As shown in Fig. 5(a), PL-CAB-10% exhibited characteristic PEO peaks after the addition of CAB, indicating that the composite solid-state electrolyte PL-CAB-10% was stable during the preparation process. Notably, the peaks corresponding to PEO in PL-CAB-10% were considerably weaker than those corresponding to PEO in PL, suggesting a reduction in the crystallinity of PEO after the addition of CAB, which improved its ability for ionic migration. Additionally, differential scanning calorimetry (DSC) analysis was performed

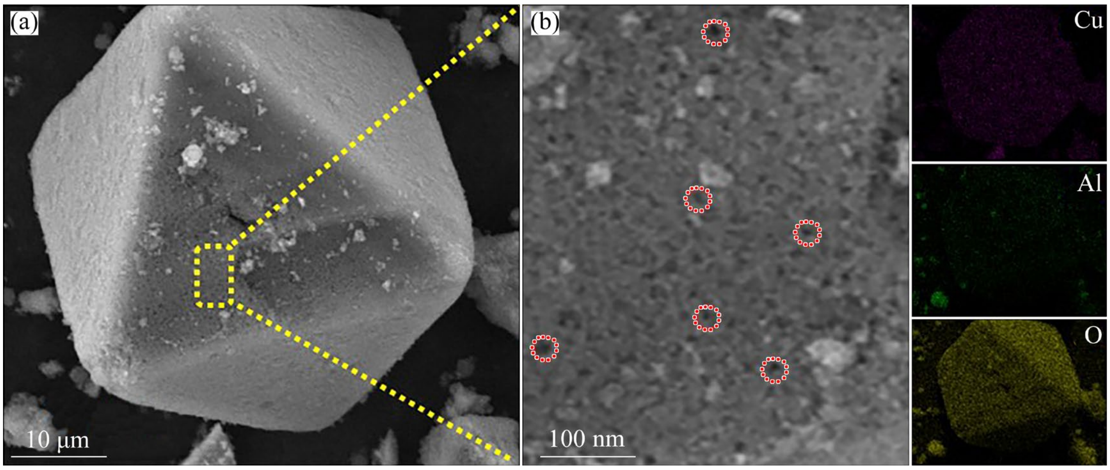

Fig. 4 SEM image (a) and partial magnification SEM image and element mapping (b) of Cu−Al bimetallic MOF

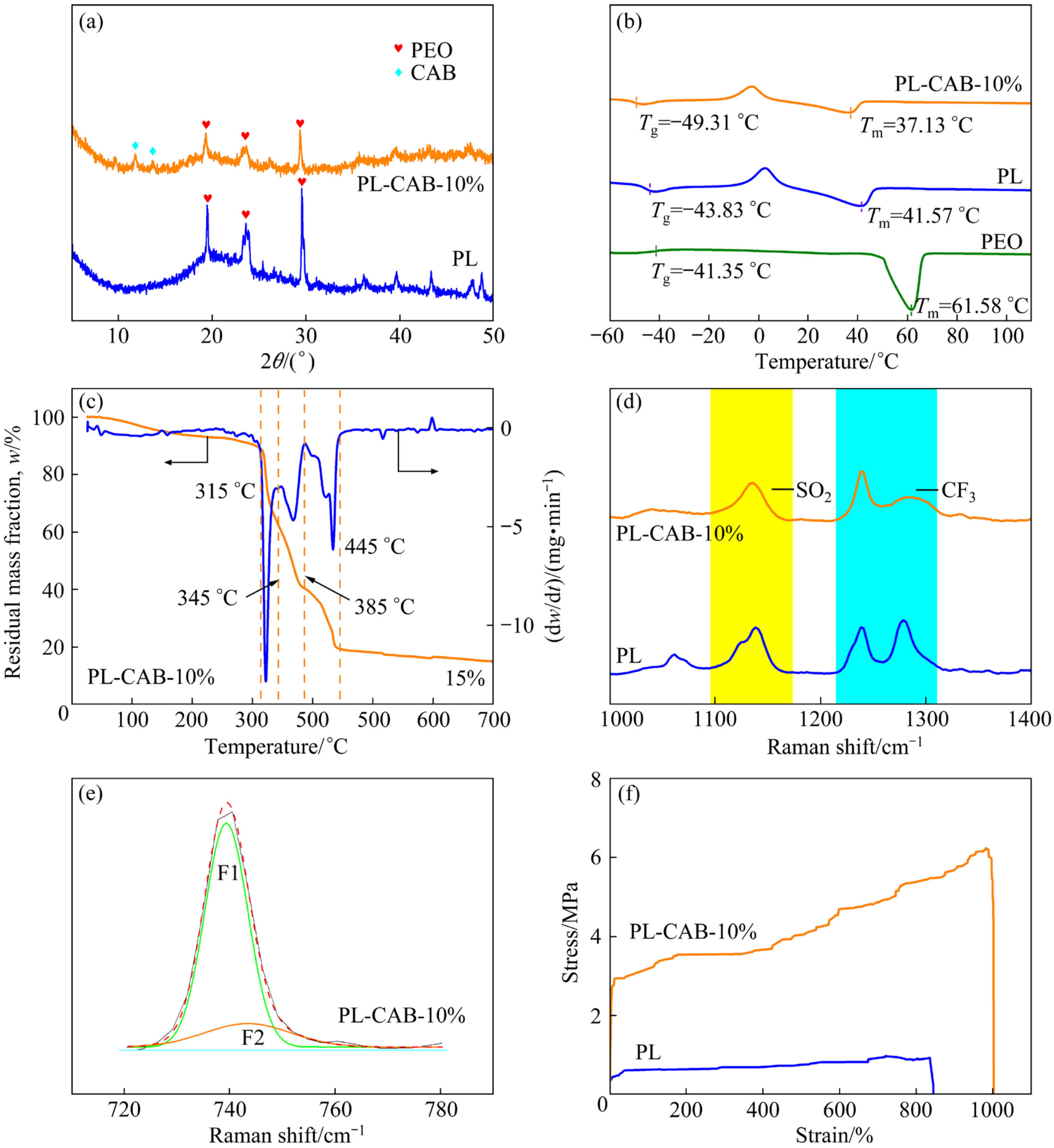

Fig. 5 XRD patterns of PL and PL-CAB-10% (a), DSC curves of PEO, PL and PL-CAB-10% (b), thermogravimetric curves of PL-CAB-10% (c), Raman spectra of PL and PL-CAB-10% (d), Raman spectra of PL-CAB-10% fitted with F1 and F2 bands (e), and stress−strain curves of PL and PL-CAB-10% (f)

to determine the glass transition temperature (T_g) and melting point (T_m) of the polymeric materials. As depicted in Fig. 5(b), the decreasing order of T_g and T_m values was PEO (T_g=−41.35 °C, T_m=61.58 °C) > PL (T_g=−43.83 °C, T_m=41.57 °C) > PL-CAB-10% (T_g=−49.31 °C, T_m=37.13 °C). Thus, the addition of LiTFSI and CAB can synergistically lower T_g and T_m of PEO, thereby enhancing its ionic conductivity. Furthermore, the proportion of crystallized regions was calculated using the melting enthalpy of the polymer materials obtained from the DSC test and Eq. (S1) in Supplementary Information [51]. The proportion of crystallized regions in PL-CAB-10% was 11.1%, lower than that of PL. Hence, incorporating CAB can improve the amorphous region in the polymeric materials, consistent with the XRD results. The decrease in the crystallized region increases the conductivity by facilitating the motion of active chain segments.

Thermogravimetric analysis (TGA) tests under an Ar atmosphere were conducted to investigate the thermal stability of the SPEs. The samples exhibited mass loss at temperatures lower than 200 °C, likely because of the desorption of surface-adsorbed water or bound water. The thermal decomposition of PEO (Fig. S2(a) in Supplementary Information) and

CAB (Fig. S2(b) in Supplementary Information) occurred within the temperature ranges of 340−420 and 280−365 °C, respectively. As shown in Fig. S2(c) in Supplementary Information, the TGA graph of PL indicated excellent stability at temperatures lower than 325 °C compared with combustible organic liquid electrolytes [52,53]. However, PL underwent an irreversible thermal decomposition occurred between 325 and 450 °C. The initial thermal decomposition temperature of PL was lower than that of pure PEO, which can be attributed to the introduction of lithium salt. By contrast, the influence of CAB on the thermal stability of PL was minimal, as depicted in Fig. 5(c). Nevertheless, a significant mass loss was observed within the temperature range of 315−445 °C, corresponding to three stages of thermal decomposition. The mass loss observed in PL-CAB-10% between 315 and 345 °C can be attributed to the decomposition process of CAB. The thermal decomposition of PEO and CAB predominated between 345 and 385 °C, while the thermal decomposition of PEO and LiTFSI dominated within the range of 385−445 °C. Ultimately, PL-CAB-10% exhibited a final residual mass fraction of 15%, higher than that of PL (8%). These TGA results indicated the excellent thermal stability of PL-CAB-10%.

Raman spectroscopy revealed characteristic peaks of $—CF_3$ and $—SO_2$ spectra within the range of 1000−1400 cm^{-1}, as illustrated in Fig. 5(d). The characteristic peaks of $—CF_3$ and $—SO_2$ considerably were weakened after the addition of CAB and can be attributed to the interaction between CAB and $TFSI^-$. As shown in Fig. 5(e) and Fig. S3 in Supplementary Information, the dissociation degree of lithium salts in PL and PL-CAB-10% was determined through Raman spectroscopy. The Lorentzian fitting curves of F1 and F2 correspond to the free $TFSI^-$ and ion cluster $[Li(TFSI)_2]^-$, respectively. The percentage of free $TFSI^-$ was calculated using Eq. (S2) in Supplementary Information [54]. The dissociation degree of lithium salt in PL-CAB-10% was 82.59%, remarkably higher than that in PL (49.74%). This increase can be primarily attributed to the addition of CAB, which possesses abundant unsaturated Cu/Al site, restricting the formation of $[Li(TFSI)_2]^-$ aggregates through Lewis acid–base interactions and thereby increasing the availability of Li^+ and $TFSI^-$.

The mechanical properties of solid-state electrolytes notably influence the safety performance of SSBs [55]. Typically, solid-state electrolyte films with poor mechanical strength are prone to puncture upon collisional deformation of the battery, leading to short circuits. The tensile strength of PL-CAB-10% reached 6.2 MPa (Fig. 5(f)), with a maximum strain of 1002%, surpassing that of PL (0.97 MPa, 845%), demonstrating good plastic flexibility. Hence, the mechanical properties of the composite solid electrolyte were improved substantially upon the addition of CAB. Furthermore, the excellent flexibility of PL-CAB-10% effectively reduced the susceptibility of the electrolyte film to rupture under external forces. Additionally, PL-CAB-10% can prevent the breakage of the solid electrolyte film due to the growth of lithium dendrites, thereby enhancing the long-cycle stability and safety performance of SSBs.

The effects of CAB filler on the morphological characteristics of the PEO-based PL and PL-CAB-10% polymer samples were analyzed through SEM. Figure 6(a) and the corresponding inset indicate uneven areas and wrinkles on the surface of the PL film. However, after incorporating CAB, PL-CAB-10% exhibited a more even, smoother, and almost wrinkle-free surface morphology, as depicted in Fig. 6(b). This even, smooth surface facilitated interface contact with the positive and negative electrodes, resulting in the uniform deposition of Li^+, and enhanced battery stability during long cycling. Furthermore, numerous holes were observed on the cross-section of the PL-CAB-10% solid electrolyte film (Fig. 6(c)), providing interfacial channels for efficient lithium-ion transport and enhancing transport efficiency. Hence, the addition of CAB improves the internal structure of the original electrolyte film. Element mappings (Fig. 6(d)) indicated the uniform distribution of Cu, N, C, Al, S, O, and F elements throughout the composite electrolyte, indicating that CAB was evenly dispersed within the polymer electrolyte rather than aggregated into clusters.

The enhancement of ionic conductivity in SPEs upon the addition of CAB was investigated through AC impedance tests conducted using blocking cells at temperatures ranging from 30 to 60 °C. The AC impedance spectra of SPEs with varying filler contents are presented in Fig. 7(a) and

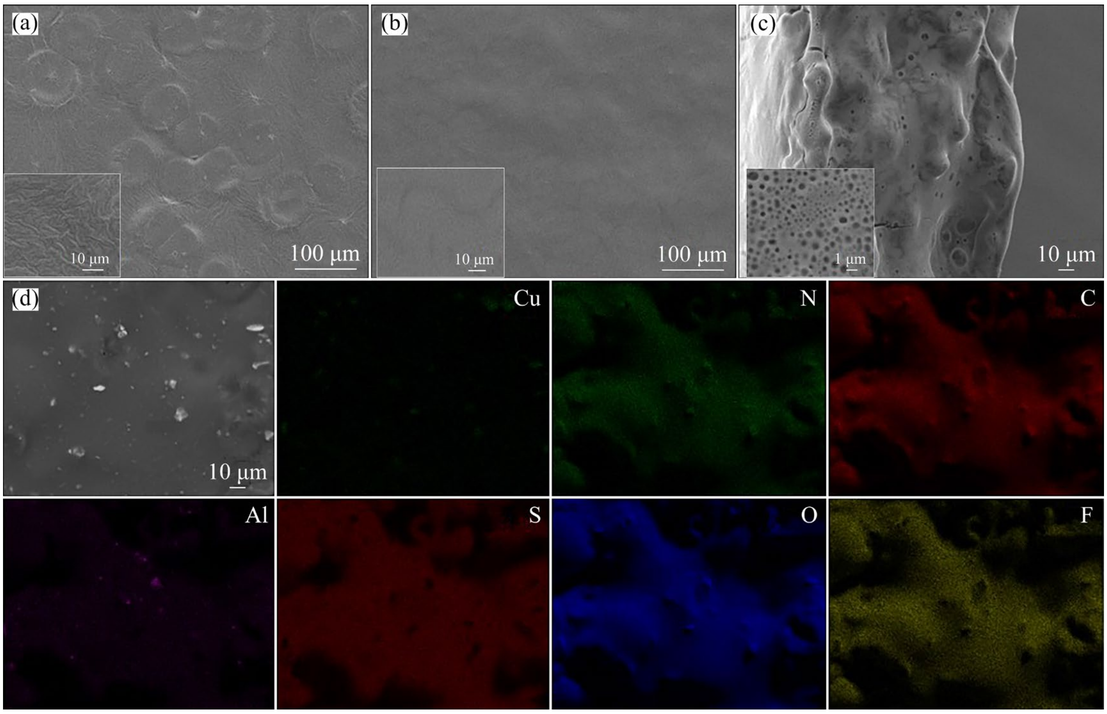

Fig. 6 SEM images of PL (a) and PL-CAB-10% (b), cross-sectional SEM image of PL-CAB-10% (c), and cross-sectional mappings of PL-CAB-10% (d)

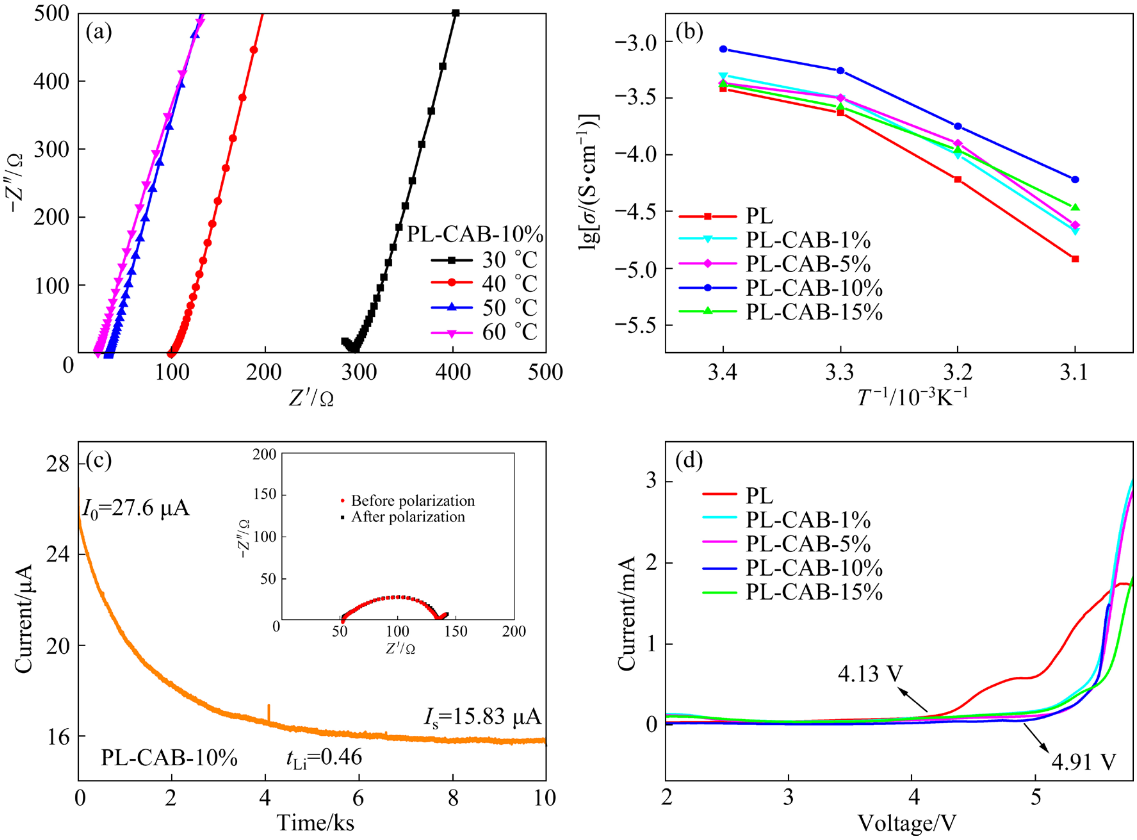

Fig. 7 AC impedance spectra of PL-CAB-10% at different temperatures (a), comparison of ionic conductivity of different samples at different temperatures (b), chronoamperometry profile of Li/PL-CAB-10%/Li symmetrical cell (inset: AC impedances of corresponding symmetric cell before and after polarization) (c), and electrochemical window curves of different samples (d)

Fig. S4 (Supplementary Information). The resistance of all SPEs decreased with increasing temperature because of the decrease in the crystallized region in the polymer matrix and the accelerated chain segment motion of the PEO chain segment at high temperatures. These factors favor the migration of lithium ions, thereby reducing the interfacial resistance of the SPEs. Conductivity tests revealed that Cu−Al bimetallic MOFs are superior to Cu-based monometallic MOF, as shown in Fig. S5 in Supplementary Information. Within the temperature range from 30 to 60 °C, the Cu−Al bimetallic MOFs exhibited higher ionic conductivity compared with the Cu-based monometallic MOF (HKUST-1). The bimetallic MOF with a Cu−Al molar ratio of 6:1 exhibited the highest ionic conductivity. Therefore, the Cu−Al bimetallic MOF with a molar ratio of 6:1 was selected as the optimal material for subsequent experiments. Figure 7(b) displays the calculated ionic conductivities of SPEs with different CAB filler contents using the AC impedance spectra at different temperatures according to Eq. (S3) in Supplementary Information. The ionic conductivities of the composite SPEs with CAB fillers were higher than that of the SPEs without CAB. Moreover, the composite solid electrolytes filled with 10% CAB filler (PL-CAB-10%) exhibited the highest ionic conductivity within the temperature range from 30 to 60 °C. However, the variation of ionic conductivity was not always linearly related to the increase in CAB filler content. The ionic conductivity of the SPEs with 10% CAB filler was the highest. However, the conductivity decreased with further increases in the CAB filler content (e.g., 15%) because of an excess of CAB filler, which aggregates and blocks the Li^+ migration pathway, thereby decreasing the ionic conductivity. The composite SPEs filled with 10% CAB filler exhibited optimal conductivities of 6.06×10^{-5} S/cm at 30 °C and 8.42×10^{-4} S/cm at 60 °C, which were considerably higher than those of PL (1.19×10^{-5} S/cm at 30 °C and 3.77×10^{-4} S/cm at 60 °C). These results indicated that adding suitable amounts of CAB filler can effectively reduce the interface resistance of the PEO-based polymers and improve their ionic conductivities.

Lithium-ion transference number (t_{Li}) is an important indicator of the electrochemical performance of SPEs. Li−Li symmetric cells were assembled using polymer electrolytes with varying CAB contents, and their transference number was calculated. Additionally, the polarization current and impedance were measured before and after polarization. By utilizing Eq. (S4) in Supplementary Information, the t_{Li} values of PL (Fig. S6(a) in Supplementary Information), PL-CAB-1% (Fig. S6(b) in Supplementary Information), PL-CAB-5% (Fig. S6(c) in Supplementary Information), PL-CAB-10% (Fig. 7(c)) and PL-CAB-15% (Fig. S6(d) in Supplementary Information) were 0.24, 0.38, 0.40, 0.46, and 0.42, respectively. The variations in t_{Li} of the polymer electrolytes were consistent with the changes in ionic conductivity (Fig. 7(b)). The interfacial channels for lithium-ion in the polymer electrolytes may be obstructed by the aggregation of excessive CAB filler, which hinders lithium-ion transport. However, an appropriate amount (10%) of CAB can facilitate lithium salt decomposition, restrict TFSI migration, and increase the lithium-ion transference number.

Linear scanning voltammetry (LSV) tests were conducted to determine the electrochemical window of the prepared electrolytes. As depicted in Fig. 7(d), the electrolytes were gradually oxidized with the increase in voltage. Pure PEO oxidized at about 4.13 V, whereas the SPEs with addition of CAB underwent oxidative decomposition at higher voltages, reaching 4.91 V. Hence, the addition of CAB can enhance the internal structure of the SPEs, enabling them to withstand high voltages without causing structural damage and widening the electrochemical window.

3.3 Cycle stability of Li−Li symmetric cells

The inhibitory effects of CAB on lithium dendrites and the stability of the solid–solid interface were analyzed through cycling tests using Li−Li symmetric cells. The stability of the output voltage under corresponding conditions indicated that the interface between the electrolyte and the electrode was stable during cycling. As illustrated in Fig. 8(a), the voltage of the Li−Li symmetric cell assembled with PL fluctuated drastically after 300 cycles at 0.1 mA/cm^2, indicating inferior interface stability. This phenomenon can be attributed to unsatisfactory interfacial contact and poor mechanical strength of the PL electrolyte. As cycling progressed, the Li^+ accumulated at the interface, resulting in lithium dendrites, decreased

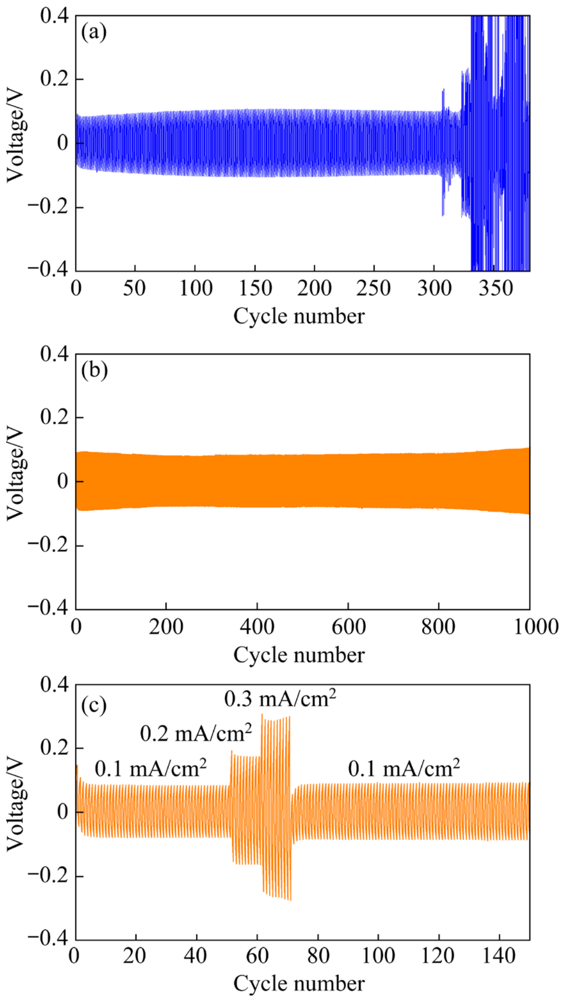

Fig. 8 Cycle performance of Li−Li symmetrical cells based on PL (a) and PL-CAB-10% (b) at current densities of 0.1 mA/cm^2, and cyclic testing results of Li−Li symmetrical cells based on PL-CAB-10% at different current densities (c)

interface stability, restricted Li$^+$ insertion/extraction, and increased interface resistance. By comparison, the Li−Li symmetric cell assembled with PL-CAB-10% (Fig. 8(b)) maintained a voltage of approximately 100 mV for 1000 cycles at 0.1 mA/cm^2, indicating superior interface stability primarily because of the incorporation of CAB. The initial voltage of the PL-CAB-10% symmetric cell was approximately 100 mV, but gradually decreased and stabilized at 70−80 mV with increasing cycles. This initial behavior can be attributed to the inadequate and unstable interfacial contact between the solid electrolyte and the electrodes during the initial cycling, which requires activation through subsequent cycles. As illustrated in Fig. 8(c), the Li−Li symmetric cell assembled with PL-CAB-10% was stable at different current densities of 0.1, 0.2, and 0.3 mA/cm^2. This can be attributed to the uniform cation plating and the generation of stable interfacial layers during the charge–discharge process, thereby enhancing the cycle stability of SSBs.

3.4 Electrochemical performance of asymmetric cells

Two asymmetric cells, $LiFePO_4$/PL/Li and $LiFePO_4$/PL-CAB-10%/Li were assembled with $LiFePO_4$ as the cathode and metallic lithium as the anode to assess the practical applicability of PL and PL-CAB-10% in SSBs. Constant-current charging at 1.0*C* (1.0*C*=170 mA/g) to 3.8 V followed by constant-voltage charging resulted in high charging efficiency and reduced charging time, without overcharging or damage of the battery at high currents. The current density of the battery during constant-current discharging was 1.0*C*. As shown in Fig. S7(a) in Supplementary Information, the $LiFePO_4$/PL/Li cell exhibited substantial capacity degradation after approximately 10 cycles, with a capacity retention rate of only 59% after 100 cycles. Additionally, its coulombic efficiency (CE) fluctuated considerably during cycling, indicating poor cycling stability. By contrast, the $LiFePO_4$/PL-CAB-10%/Li cell exhibited an initial discharge capacity of 155.9 mA·h/g, with a capacity retention rate of 92.7% after 100 cycles, as shown in Fig. 9(a). Furthermore, the charge/discharge voltage plateau of the $LiFePO_4$/PL-CAB-10%/Li cell remained stable throughout cycling (Fig. 9(b)), with a smaller voltage of approximately 0.20 V compared with PL (about 1.05 V in Fig. S7(b) in Supplementary Information), indicating excellent cyclic stability and reduced electrochemical polarization.

The interfacial stability of the $LiFePO_4$/PL/Li and $LiFePO_4$/PL-CAB-10%/Li cells after 100 cycles was analyzed through AC impedance tests, as illustrated in Figs. S8(a) and S8(b) in Supplementary Information, respectively. The resistance of the $LiFePO_4$/PL-CAB-10%/Li cell was lower than 800 Ω after 100 cycles. By contrast, the resistance of the $LiFePO_4$/PL/Li cell was in the order of tens of ohms, likely because of interfacial instability, resulting in poor electrochemical performance; whereas, PL-CAB-10% improved interfacial stability during cycling owing to the introduction of CAB.

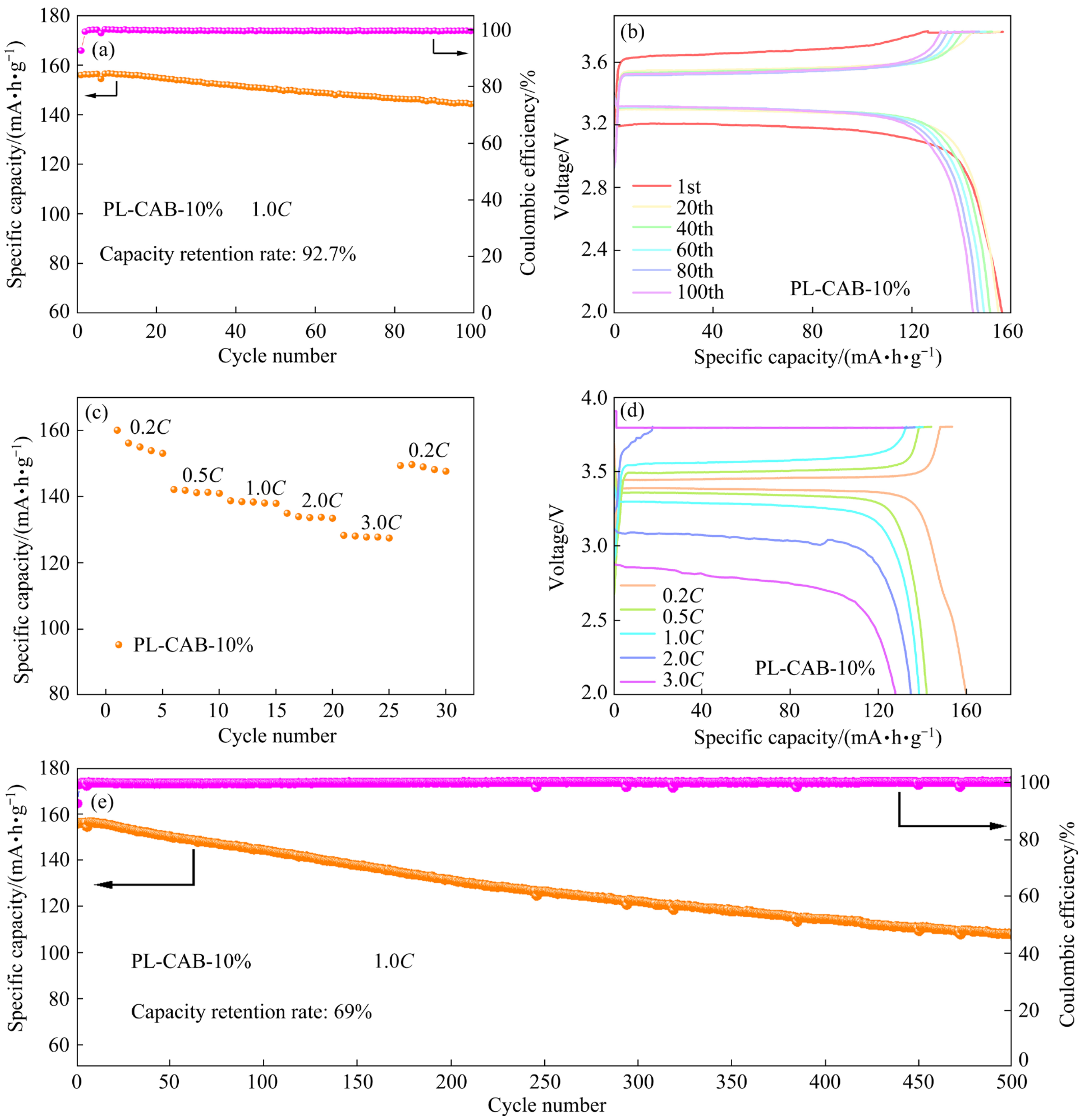

Fig. 9 Electrochemical performances of $LiFePO_4$/PL-CAB-10%/Li: (a, b) Cycling performance at 1.0*C* and corresponding charge/discharge voltage profiles at different cycles, respectively; (c, d) Rate performance from 0.2*C* to 3.0*C* and corresponding charge/discharge voltage profiles at different rates, respectively; (e) Long-term cycle performance at 1.0*C*

The rate performance of the $LiFePO_4$/PL-CAB-10%/Li cell was evaluated within the range of 0.2*C*−3.0*C*, as shown in Fig. 9(c). The specific capacities obtained at 0.2*C*, 0.5*C*, 1.0*C*, 2.0*C*, and 3.0*C* were 156.1, 141.8, 138.7, 134.9, and 128.2 mA·h/g, respectively. As illustrated in Fig. 9(d), the discharge plateaus of $LiFePO_4$/PL-CAB-10%/Li gradually decreased with the increase in the current density from 3.0*C* to 0.2*C*, whereas the charging plateaus gradually increased, indicating increased electrochemical polarization. However, even when the current density returned to 0.2*C*, the specific capacity remained stable at 149.6 mA·h/g, with a relatively high retention rate of 95.8% compared with the initial discharge specific capacity. Furthermore, $LiFePO_4$/PL-CAB-10%/Li exhibited a discharge capacity of over 100 mA·h/g at a high rate of 5.0*C* (Fig. S9 in Supplementary Information). When the rate returned to 0.5*C*, a retention rate as high as 93.7% was achieved, indicating that the rate performance of $LiFePO_4$/PL-CAB-10%/Li was favorable.

Furthermore, the long cycling life of $LiFePO_4$/PL-CAB-10%/Li was measured and presented in Fig. 9(e). $LiFePO_4$/PL-CAB-10%/Li maintained a discharge capacity of approximately 110 mA·h/g after 500 cycles, with a capacity retention rate of 70%. The corresponding CE remained about 100%, indicating outstanding long cycling performance. Moreover, the cycling performance of $LiFePO_4$/PL-CAB-10%/Li was superior to those of previously reported electrolyte materials (Table S1 in Supplementary Information). The improved electrochemical performance of PL-CAB-10% can be primarily attributed to the addition of Cu−Al bimetallic MOF, which provides abundant Lewis acid metal sites and regular pore channels, leading to increased Li^+ transference number, ionic conductivity, and interfacial stability during cycling. Figure 10 briefly illustrates the influence mechanism of PL-CAB-10% incorporated through molecular grafting.

3.5 Molecular dynamics simulation

Molecular dynamics simulation (MDS) is a crucial and reliable technique for analyzing the macroscopic physicochemical properties and microscopic mechanisms of solid-state electrolytes [56,57]. MDS snapshots of PL and PL-CAB are plotted in Fig. S1(d) (Supplementary Information) and Fig. 11(a), respectively. The amorphous segments and Li^+ diffusivity of the SPEs system can be determined by evaluating the value of T_g. The average densities of the SPEs system were calculated under temperature variations from 400 to 160 K, with intervals of 20 K, using the MDS module. The variations in the specific volume of the PL and PL-CAB systems with changes in temperature are depicted in Fig. S10 in Supplementary Information and Fig. 11(b), respectively. The specific volume increased with the increase of temperature, but the variation rates differed throughout the temperature range. T_g of the system was evaluated by determining the slope of the specific volume versus temperature curve that represented the transition of the solid-state electrolyte from the glassy state to the rubbery state. The calculated T_g value of PL-CAB was 218.57 K (−54.58 °C), generally consistent with the DSC results of −49.31 °C. Furthermore, the T_g value of PL-CAB was considerably lower than that of PL (T_g=241.25 K), indicating a larger number of amorphous segments in PL-CAB [58,59]. This can be attributed to the introduction of CAB, which effectively increased the amorphous regions in the PEO polymer, thereby enhancing Li^+ transport in PL-CAB.

The mean square displacement (MSD) was calculated based on the Einstein formula (Eq. S(5) in Supplementary Information) to further track ionic motion in the solid-state electrolyte system. The MSD represents the distance between the initial position and the position at any moment during ion diffusion in the system. The diffusion coefficient (D) value is obtained as one-sixth of the slope of the MSD function. Figures S11 and S12 in Supplementary Information display the MSD curves of PL and PL-CAB at different temperatures, respectively; the slops of the MSD curves were obtained through linear fitting. As illustrated in Fig. 11(c), incorporating CAB significantly increased the D value of PL-CAB. Additionally, the ionic conductivities (σ) of PL and PL-CAB can be calculated using the Nernst−Einstein equation

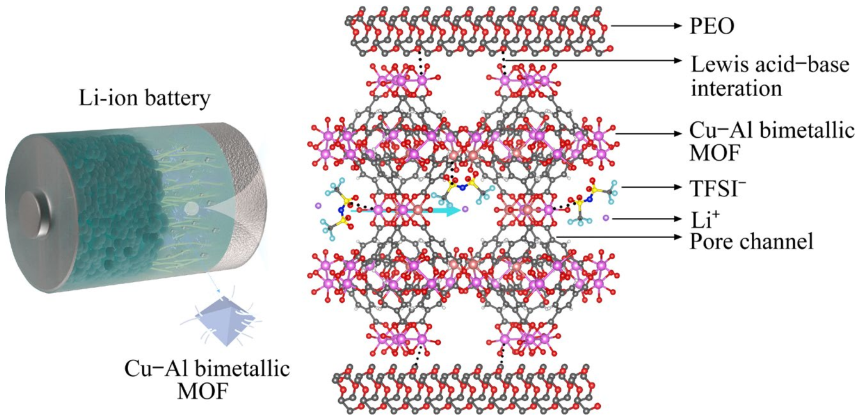

Fig. 10 Mechanism diagram of Cu−Al bimetallic MOFs reinforced PEO solid electrolyte

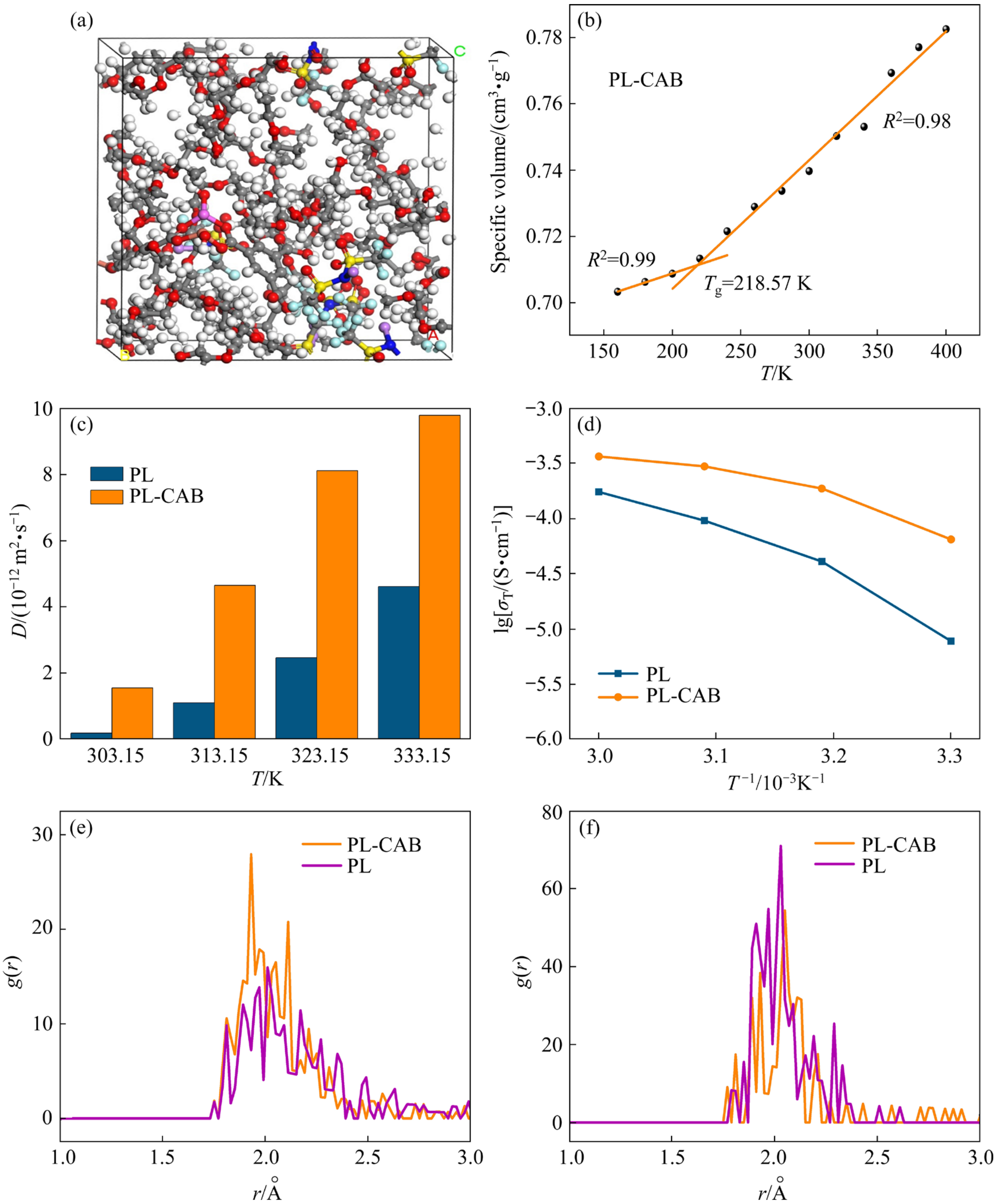

Fig. 11 MDS snapshot of PL-CAB (a), fitted glass transition temperature simulations of PL-CAB (b), comparison of diffusion coefficients (c) and ionic conductivity (d) of PL and PL-CAB obtained by calculation, and comparison of Li−O (e) and Li−O−S (f) RDF curves for PL and PL-CAB (*r* is atom spacing)

(Eq. S(6) in Supplementary Information), as shown in Fig. 11(d). The ionic conductivity of both PL and PL-CAB increased with the increase of temperature, indicating the significant influence of temperature on ionic conductivity. This was consistent with the variation in the ion diffusion coefficient with temperature (Fig. 11(c)). Notably, the ionic conductivity of PL-CAB was substantially higher than that of PL at all temperatures. At 333.15 K, the ionic conductivity of PL-CAB was as high as 3.67×10^{-4} S/cm, indicating that the PL-CAB system was not damaged, and the interfacial channels formed between the CAB and PEO polymer were maintained even at high temperatures.

The radial distribution function (RDF, *g*(*r*)) analysis was conducted to evaluate the interaction between Li and O in the PEO chain segment (Li−O) or the lithium salt (Li−O−S). Corresponding to the Li−O interaction (Fig. 11(e)), a strong peak was observed in the PL-CAB system at approximately

1.9 Å, significantly higher than that in the PL system. Hence, the interaction between Li and O in the PEO chain segment in the PL-CAB system is more likely than that in the PL system. This can be attributed to the addition of Cu−Al bimetallic MOF, which reacts with the lithium salt to dissociate more Li^+ in the PEO electrolyte. Moreover, the interfacial regions formed by CAB and PEO provided unique pathways for Li^+ motion, increasing the density of Li^+ carriers in the PEO chain segment. Consequently, the chance of interaction between Li and O in the PEO chain segment was enhanced after adding CAB. A strong peak was observed in the RDF curve of Li−O−S system, indicating a higher probability of interaction between Li and $TFSI^-$ and a lower Li^+ concentration in the system. In terms of the Li−O−S interaction (Fig. 11(f)), a peak at around 2.0 Å in the PL-CAB system was lower than that in the PL system, indicating that the dissociation of LiTFSI was enhanced after the addition of CAB. This finding was consistent with the Raman spectra (Fig. 5(e)).

4 Conclusions

(1) A polymer solid electrolyte comprising Cu−Al bimetallic MOF, LiTFSI and PEO was developed through molecular grafting. Furthermore, the incorporation of CAB improved the ionic conductivity, lithium-ion transference number, electrochemical window, thermoelectric stability, and mechanical strength of the as-prepared electrolyte.

(2) PL-CAB-10% exhibited optimal electrochemical performances. A symmetric Li−Li cell with PL-CAB-10% exhibited stable performance over 1000 cycles at 0.1 mA/cm^2, and an asymmetric $LiFePO_4$/PL-CAB-10%/Li cell exhibited a high discharge capacity of 155.9 mA·h/g with a higher retention rate of approximately 70% after 500 cycles.

(3) The enhanced physicochemical properties can be attributed to the interaction between the Lewis acidic sites of CAB and LiTFSI, the grafting effect of CAB on PEO chains, and the confinement effect of $TFSI^-$ anions in the pore structure of CAB.

CRediT authorship contribution statement

Liu-bin SONG: Conceptualization, Methodology, Data curation, Writing − Original draft preparation, Writing − Reviewing and editing, Modifying the manuscript; **Tian-yuan LONG**: Investigation; **Min-zhi XIAO**: Resources; **Min LIU**: Investigation, Replying to review comments, Modifying the manuscript; **Ting-ting**, **Yin-jie KUANG** and **Lin JIANG:** Investigation; **Zhong-liang XIAO:** Supervision, Writing − Reviewing and editing.

Declaration of competing interest

The authors declare that they have no known competing financial interests or personal relationships that could have appeared to influence the work reported in this paper.

Acknowledgments

This work was supported by the National Natural Science Foundation of China (No. 21501015), the Hunan Provincial Natural Science Foundation, China (No. 2022JJ30604), and Hunan Provincial Key Laboratory of Materials Protection for Electric Power and Transportation, China (No. 2022CL01).

Supplementary Information

Supplementary Information in this paper can be found at: http://tnmsc.csu.edu.cn/download/16-p2943-2023-0263-Supplementary_Information.pdf.

References

[1] NITTA N, WU F X, LEE J T, YUSHIN G. Li-ion battery materials: Present and future [J]. Materials Today, 2015, 18(5): 252−264.

[2] LIU Xue-ping, XIAO Zhe, PENG Hua-rong, JIANG Dong-ting, XIE Hong-gui, SUN Yi-ling, ZHONG Sheng-kui, QIAN Zheng-fang, WANG Ren-heng. Rational design of LLZO/polymer solid electrolytes for solid-state batteries [J]. Chemistry: An Asian Journal, 2022, 17(24): e202200929.

[3] YANG Jian, ZHOU Yuan, ZHANG Zong-liang, XU Kai-hua, ZHANG Kun, LAI Yan-qing, JIANG Liang-xing. Effect of electric field on leaching valuable metals from spent lithium-ion batteries [J]. Transactions of Nonferrous Metals Society of China, 2023, 33(2): 632−641.

[4] TONG Z Z, WANG S B, JENA A, LIU C E, LIAO S C, CHEN J M, CHANG H, HU S F, GUO X X, LIU R S. Matchmaker of marriage between a Li metal anode and NASICON-structured solid-state electrolyte: Plastic crystal electrolyte and three-dimensional host structure [J]. ACS Applied Materials & Interfaces, 2020, 12(40): 44754−44761.

[5] NIE Yan-mei, DAI Xiang-yu, WANG Jie-xi, QIAN Zheng-fang, WANG Zhi-xing, GUO Hua-jun, YAN Guo-chun, JIANG Dong-ting, WANG Ren-heng. Facile and scalable fabrication of lithiophilic Cu_xO enables stable lithium metal anode [J]. Journal of Energy Chemistry, 2022, 75: 285−292.

[6] GUO Zhi-hao, LI Xin-hai, WANG Zhi-xing, GUO Hua-jun, PENG Wen-jie, HU Qi-yang, YAN Guo-chun, WANG Jie-xi. Empirical decay relationship between ionic conductivity and porosity of garnet type inorganic solid-state electrolytes [J]. Transactions of Nonferrous Metals Society of China, 2022, 32(10): 3362−3373.

[7] LI Song, ZHANG Shi-qi, SHEN Lu, LIU Qi, MA Jia-bin, LV Wei, HE Yan-bing, YANG Quan-hong. Progress and perspective of ceramic/polymer composite solid electrolytes for lithium batteries [J]. Advanced Science, 2020, 7(5): 1903088.

[8] LI Tao, LI Yan, SUN Yi-ling, QIAN Zheng-fang, WANG Ren-heng. New insights on the good compatibility of ether-based localized high-concentration electrolyte with lithium metal [J]. ACS Materials Letters, 2021, 3(6): 838−844.

[9] SUN Yi-yang, WANG Jia-lu, FU Dao-song, ZHANG Feng-rui, WANG Zhi-cheng, CHEN Xi, XU Jing-jing, HU Jian-chen, WU Xiao-dong. Flexible composite solid electrolyte with an active inorganic filler [J]. ACS Sustainable Chemistry & Engineering, 2021, 9(5): 2237−2245.

[10] HE Han-bing, LIU Zhen, PENG Chao-qun, LIU Jun, WANG Xiao-feng, ZENG Jing. 3D MoS_2/graphene nanoflowers as anode for advanced lithium-ion batteries [J]. Transactions of Nonferrous Metals Society of China, 2022, 32(12): 4041−4049.

[11] UMESHBABU E, ZHENG Bi-zhu, ZHU Jian-ping, WANG Hong-chun, LI Yi-xiao, YANG Yong. Stable cycling lithium−sulfur solid batteries with enhanced Li/$Li_{10}GeP_2S_{12}$ solid electrolyte interface stability [J]. ACS Applied Materials & Interfaces, 2019, 11(20): 18436−18447.

[12] LIU Zhong-xiu, HA Si-hu, LIU Yong, WANG Fei, TAO Feng, XU Bin-rui, YU Ren-hong, WANG Guang-xin, REN Feng-zhang, LI Hong-xia. Application of Ag-based materials in high-performance lithium metal anode: A review [J]. Journal of Materials Science & Technology, 2023, 133: 165−182.

[13] KRAVCHYK K V, KOVALENKO M V. Perspective on design and technical challenges of Li-garnet solid-state batteries [J]. Science and Technology of Advanced Materials, 2022, 23(1): 41−48.

[14] FU Fang, ZHENG Yue, JIANG Nan, LIU Ying, SUN Chen, ZHANG Ao-tian, TENG Hong, SUN Li-qun, XIE Hai-ming. A dual-salt PEO-based polymer electrolyte with cross-linked polymer network for high-voltage lithium metal batteries [J]. Chemical Engineering Journal, 2022, 450(1): 137776.

[15] NIE Kai-hui, HONG Yan-shuai, QIU Ji-liang, LI Qing-hao, YU Xi-qian, LI Hong, CHEN Li-quan. Interfaces between cathode and electrolyte in solid state lithium batteries: Challenges and perspectives [J]. Frontiers in Chemistry, 2018, 6: 616.

[16] WANG Chun-hua, BAI Guo-liang, LIU Xing-jiang, LI Yang. Favorable electrochemical performance of $LiMn_2O_4$/$LiFePO_4$ composite electrodes attributed to composite solid electrolytes for all-solid-state lithium batteries [J]. Langmuir, 2021, 37(7): 2349−2354.

[17] LIU Ke, ZHANG Rui-han, SUN Jing, WU Mao-chun, ZHAO Tian-shou. Polyoxyethylene (PEO)|PEO−perovskite|PEO composite electrolyte for all-solid-state lithium metal batteries [J]. ACS Applied Materials & Interfaces, 2019, 11(50): 46930−46937.

[18] LI Zhen, ABOALSAUD A M, LIU Xiao-wei, THANKAMONY R L, CHEN I C, LI Yang-xing, LAI Zhi-ping. Scalable fabrication of solvent-free composite solid electrolyte by a continuous thermal-extrusion process [J]. Journal of Colloid and Interface Science, 2022, 628: 64−71.

[19] BONILLA M R, GARCIA DAZA F A, CORTES H A, CARRASCO J, AKHMATSKAYA E. On the interfacial lithium dynamics in $Li_7La_3Zr_2O_{12}$: Poly(ethylene oxide) (LiTFSI) composite polymer-ceramic solid electrolytes under strong polymer phase confinement [J]. Journal of Colloid and Interface Science, 2022, 623: 870−882.

[20] LIU Hai-ling, MULDERRIG L, HALLINAN D Jr, CHUNG Ho-yong. Lignin-based solid polymer electrolytes: Lignin-graft-poly(ethylene glycol) [J]. Macromolecular Rapid Communications, 2021, 42(3): 2170007.

[21] ZHANG Feng-rui, SUN Yi-yang, WANG Zhi-cheng, FU Dao-song, LI Jing, HU Jian-chen, XU Jing-jing, WU Xiao-dong. Highly conductive polymeric ionic liquid electrolytes for ambient-temperature solid-state lithium batteries [J]. ACS Applied Materials & Interfaces, 2020, 12(21): 23774−23780.

[22] ZHUANG Hua, MA Wen-cheng, XIE Jing-wei, LIU Xiao-yu, LI Bo-bo, JIANG Yong, HUANG Shou-shuang, CHEN Zhi-wen, ZHAO Bing. Solvent-free synthesis of PEO/garnet composite electrolyte for high-safety all-solid-state lithium batteries [J]. Journal of Alloys and Compounds, 2021, 860: 157915.

[23] ZHAO Yan-ran, WU Chuan, PENG Gang, CHEN Xiao-tian, YAO Xia-yin, BAI Ying, WU Feng, CHEN Shao-jie, XU Xiao-xiong. A new solid polymer electrolyte incorporating $Li_{10}GeP_2S_{12}$ into a polyethylene oxide matrix for all-solid-state lithium batteries [J]. Journal of Power Sources, 2016, 301: 47−53.

[24] KATO M, HIRAOKA K, SEKI S. Investigation of the ionic conduction mechanism of polyether/$Li_7La_3Zr_2O_{12}$ composite solid electrolytes by electrochemical impedance spectroscopy [J]. Journal of the Electrochemical Society, 2020, 167(7): 070559.

[25] LI Xiao-long, WANG Xian-you, SHAO Ding-sheng, LIU Lei, YANG Li. Preparation and performance of poly(ethylene oxide)-based composite solid electrolyte for all solid-state lithium batteries [J]. Journal of Applied Polymer Science, 2019, 136(19): 47498.

[26] LIN D C, LIU W, LIU Y Y, LEE H R, HSU P C, LIU K, CUI Y. High ionic conductivity of composite solid polymer electrolyte via in situ synthesis of monodispersed SiO_2 nanospheres in poly(ethylene oxide) [J]. Nano Letters, 2016, 16(1): 459−465.

[27] LIM Y J, AN Y H, JO N J. Polystyrene−Al_2O_3 composite solid polymer electrolyte for lithium secondary battery [J]. Nanoscale Research Letters, 2012, 7: 19.

[28] SHENG Ou-wei, JIN Cheng-bin, LUO Jian-min, YUAN Hua-dong, HUANG Hui, GAN Yong-ping, ZHANG Jun, XIA Yang, LIANG Chu, ZHANG Wen-kui, TAO Xin-yong. $Mg_2B_2O_5$ nanowire enabled multifunctional solid-state

electrolytes with high ionic conductivity, excellent mechanical properties, and flame-retardant performance [J]. Nano Letters, 2018, 18(5): 3104−3112.

[29] ZHANG Yi, WANG Xiao-hui, FENG Wei, ZHEN Yi-chao, CAI Zi-ming, LI Long-tu. Effects of the shapes of $BaTiO_3$ nanofillers on PEO-based electrolytes for all-solid-state lithium-ion batteries [J]. Ionics, 2019, 25(4): 1471−1480.

[30] WU N, CHIEN P H, QIAN Y M, LI Y T, XU H H, GRUNDISH N S, XU B Y, JIN H B, HU Y Y, YU G H, GOODENOUGH J B. Enhanced surface interactions enable fast Li^+ conduction in oxide/polymer composite electrolyte [J]. Angewandte Chemie: International Edition, 2020, 59(10): 4131−4137.

[31] ZHAO Ruo, WU Ying-xiao, LIANG Zi-bin, GAO Lei, XIA Wei, ZHAO Yu-sheng, ZOU Ru-qiang. Metal-organic frameworks for solid-state electrolytes [J]. Energy & Environmental Science, 2020, 13: 2386−2403.

[32] HE Han-bing, LI Ren, YANG Zhi-hui, CHAI Li-yuan, JIN Lin-feng, ALHASSAN S I, REN Li-li, WANG Hai-ying, HUANG Lei. Preparation of MOFs and MOFs derived materials and their catalytic application in air pollution: A review [J]. Catalysis Today, 2021, 375: 10−29.

[33] LU Guo-long, WEI Hong-jin, SHEN Chuan-qi, ZHOU Feng, ZHANG Min, CHEN Yi-huang, JIN Hui-le, LI Jun, CHEN Guang, WANG Ji-chang, WANG Shun. Bifunctional MOF doped PEO composite electrolyte for long-life cycle solid lithium ion battery [J]. ACS Applied Materials & Interfaces, 2022, 14(40): 45476−45483.

[34] HE Wen-chao, LI Di-xiong, GUO Si-jia, XIAO Ying-bo, GONG Wei, ZENG Qing-han, OUYANG Yuan, LI Xin, DENG Hao-yan, TAN Chao, ZHANG Qi, HUANG Shao-ming. Redistribution of electronic density in channels of metal-organic frameworks for high-performance quasi-solid lithium metal batteries [J]. Energy Storage Materials, 2022, 47: 271−278.

[35] MASOOMI M Y, MORSALI A, DHAKSHINAMOORTHY A, GARCIA H. Mixed-metal MOFs: Unique opportunities in metal-organic framework (MOF) functionality and design [J]. Angewandte Chemie: International Edition, 2019, 58(43): 15188−15205.

[36] FENG Liang, WANG Kun-yu, DAY G S, ZHOU Hong-cai. The chemistry of multi-component and hierarchical framework compounds [J]. Chemical Society Reviews, 2019, 48(18): 4823−4853.

[37] CHEN Li-yu, WANG Hao-Fan, LI Cai-xia, XU Qiang. Bimetallic metal-organic frameworks and their derivatives [J]. Chemical Science, 2020, 11(21): 5369−5403.

[38] SUN Chang-chun, YUSUF A, LI Shao-wen, QI Xiao-lin, MA Yue, WANG De-yi. Metal organic frameworks enabled rational design of multifunctional PEO-based solid polymer electrolytes [J]. Chemical Engineering Journal, 2021, 414: 128702.

[39] SHEN Kui, CHEN Xiao-dong, CHEN Jun-ying, LI Ying-wei. Development of MOF-derived carbon-based nanomaterials for efficient catalysis [J]. ACS Catalysis, 2016, 6(9): 5887−5903.

[40] SHI Yong, CHU Qi, NIU Dan-yang, WU Zhuo-min, HUANG Lei. Synthesis and characterization of bimetallic Cu−Al-BTC MOFs as an efficient catalyst for selective catalysis reduction of NO with CO [J]. Ferroelectrics, 2020, 565(1): 58−65.

[41] ZHANG Xiao, SHEN Bo-xiong, ZHANG Xiao-qi, WANG Fu-mei, CHI Gui-long, SI Meng. A comparative study of manganese-cerium doped metal-organic frameworks prepared via impregnation and in situ methods in the selective catalytic reduction of NO [J]. RSC Advances, 2017, 7(10): 5928−5936.

[42] JIANG Hao-xi, NIU Ying, WANG Qian-yun, CHEN Yi-fei, ZHANG Min-hua. Single-phase SO_2-resistant to poisoning Co/Mn-MOF-74 catalysts for NH_3-SCR [J]. Catalysis Communications, 2018, 113: 46−50.

[43] BROZEK C K, COZZOLINO A F, TEAT S J, CHEN Y S, DINCA M. Quantification of site-specific cation exchange in metal-organic frameworks using multi-wavelength anomalous X-ray dispersion [J]. Chemistry of Materials, 2013, 25(15): 2998−3002.

[44] DAS S, KIM H, KIM K. Metathesis in single crystal: Complete and reversible exchange of metal ions constituting the frameworks of metal-organic frameworks [J]. Journal of the American Chemical Society, 2009, 131(11): 3814−3815.

[45] REINSCH H, KRUEGER M, WACK J, SENKER J, SALLES F, MAURIN G, STOCK N. A new aluminium-based microporous metal-organic framework: Al(BTB) (BTB=1, 3, 5-benzenetrisbenzoate) [J]. Microporous and Mesoporous Materials, 2012, 157: 50−55.

[46] MA Sheng-xiang, SHEN Li, LIU Qian, SHI Wen-yue, ZHANG Chen, LIU Fang, BAUCOM J A, ZHANG Dong, YUE Hui-juan, WU Hao-bin, LU Yun-feng. Class of solid-like electrolytes for rechargeable batteries based on metal-organic frameworks infiltrated with liquid electrolytes [J]. ACS Applied Materials & Interfaces, 2020, 12(39): 43824−43832.

[47] YANG Xin-chun, XU Qiang. Bimetallic metal−organic frameworks for gas storage and separation [J]. Crystal Growth & Design, 2017, 17(4): 1450−1455.

[48] RICE A M, LEITH G A, EJEGBAVWO O A, DOLGOPOLOVA E A, SHUSTOVA N B. Heterometallic metal−organic frameworks (MOFs): The advent of improving the energy landscape [J]. ACS Energy Letters, 2019, 4(8): 1938−1946.

[49] CHUI S S Y, LO S M F, CHARMANT J P H, ORPEN A G. A chemically functionalizable nanoporous material $[Cu_3(TMA)_2(H_2O)_3]_n$ [J]. Science, 1999, 283: 1148−1150.

[50] SHEN Li, WU Hao-bin, LIU Fang, BROSMER J L, SHEN Gu-rong, WANG Xiao-feng, ZINK J I, XIAO Qiang-feng, CAI Mei, WANG Ge, LU Yun-feng, DUNN B. Creating lithium-ion electrolytes with biomimetic ionic channels in metal-organic frameworks [J]. Advanced Materials, 2018, 30(23): 1707476.

[51] OLMEDO-MARTINEZ J L, MEABE L, RIVA R, GUZMAN-GONZALEZ G, PORCARELLI L, FORSYTH M, MUGICA A, CALAFEL I, MULLER A J, LECOMTE P, JEROME C, MECERREYES D. Flame retardant polyphosphoester copolymers as solid polymer electrolyte for lithium batteries [J]. Polymer Chemistry, 2021, 12(23): 3441−3450.

[52] DING Chen-feng, FU Xue-wei, LI Hao, YANG Jia-yi, YU Yun-hua, ZHONG Wei-hong, YANG Xiao-ping. An

ultrarobust composite gel electrolyte stabilizing ion deposition for long-life lithium metal batteries [J]. Advanced Functional Materials, 2019, 29(43): 1904547.

[53] LV Fei, WANG Zhu-yi, SHI Li-yi, ZHU Jie-fang, EDSTROM K, MINDEMARK J, YUAN Shuai. Challenges and development of composite solid-state electrolytes for high-performance lithium ion batteries [J]. Journal of Power Sources, 2019, 441: 227175.

[54] HUO Han-yu, WU Bin, ZHANG Tao, ZHENG Xu-sheng, GE Liang, XU Tong-wen, GUO Xiang-xin, SUN Xue-liang. Anion-immobilized polymer electrolyte achieved by cationic metal-organic framework filler for dendrite-free solid-state batteries [J]. Energy Storage Materials, 2019, 18: 59−67.

[55] KE X Y, WANG Y, REN G F, YUAN C. Towards rational mechanical design of inorganic solid electrolytes for all-solid-state lithium ion batteries [J]. Energy Storage Materials, 2020, 26: 313−324.

[56] NOLAN A M, ZHU Yi-zhou, HE Xing-feng, BAI Qiang, MO Yi-fei. Computation-accelerated design of materials and interfaces for all-solid-state lithium-ion batteries [J]. Joule, 2018, 2(10): 2016−2046.

[57] ZHU Yi-zhou, HE Xing-feng, MO Yi-fei. Origin of outstanding stability in the lithium solid electrolyte materials: Insights from thermodynamic analyses based on first-principles calculations [J]. ACS Applied Materials & Interfaces, 2015, 7(42): 23685−23693.

[58] WU Xiao-xue, CHEN Ke-yi, YAO Zhen-guo, HU Jiu-lin, HUANG Min-song, MENG Jun-wei, MA Shi-ping, WU Tao, CUI Yan-hua, LI Chi-lin. Metal organic framework reinforced polymer electrolyte with high cation transference number to enable dendrite-free solid state Li metal conversion batteries [J]. Journal of Power Sources, 2021, 501: 229946.

[59] MOHAMADI M. Interpretation of thermal transitions and phase transformations in semi-crystalline PVDF/PEO/graphene nanocomposites characterized by modulated-temperature DSC [J]. Journal of Thermal Analysis and Calorimetry, 2022, 147(12): 6701−6712.

基于 Cu−Al 双金属有机框架的分子接枝提高固体聚合物电解质的离子电导率

宋刘斌[1,2]，龙田源[1]，肖敏之[1]，刘敏[3]，赵亭亭[1,2]，匡尹杰[1,2]，蒋琳[1]，肖忠良[1,2]

1. 长沙理工大学 化学与化学工程学院，长沙 410114；
2. 长沙理工大学 电力与交通材料保护湖南省重点实验室，长沙 410114；
3. 宁波工程学院 新能源学院，宁波 315336

摘　要：为了提高聚环氧乙烷(PEO)基电解质的离子电导率，通过分子接枝工程制备了一种由 Cu−Al 双金属有机框架(CAB)、锂盐(LiTFSI)和聚环氧乙烷 PEO 组成的复合固体电解质。实验和分子动力学模拟结果表明，含有 10% CAB(质量分数)的电解质(PL-CAB-10%)具有较高的离子电导率(60 ℃时为 8.42×10^{-4} S/cm)、较大的 Li^+转移数(0.46)、较宽的电化学窗口(4.91 V)、良好的热稳定性和优异的力学性能。此外，PL-CAB-10%在 Li−Li 对称电池和 Li/PL-CAB-10%/$LiFePO_4$ 非对称电池中均表现出优异的循环稳定性。其性能提升主要归因于多功能 CAB 的引入。CAB 中的丰富金属位点可以通过 Lewis 酸碱相互作用与 $TFSI^-$和 PEO 反应，这既促进了 LiTFSI 的解离，又提高了离子电导率。同时，CAB 中的规则孔洞为阳离子均匀涂覆提供了均一的分散位点。

关键词：聚环氧乙烷；铜铝双金属有机框架；固体锂金属电池；分子接枝；离子电导率

(Edited by Wei-ping CHEN)